Insights into the microscopic mechanism of persistent luminescence in Cr^{3+}-doped $ZnGa_2O_4$ phosphors

Dingjun Jia,[a] Wenna Gao,[a] Wenqian Xu,[a] Xiangyu Zhang*[b] and Dangli Gao*[a]

[a] China College of Science, Xi'an University of Architecture and Technology, Xi'an, Shaanxi 710055, China. E-mail: gaodangli@163.com, gaodangli@xauat.edu.cn

[b] College of Science, Chang'an University, Xi'an, Shaanxi 710064, China. E-mail: xyzhang@chd.edu.cn

Table S1. Cr^{3+} activated afterglow phosphors.

Host Material	Activator	Co-dopant	Afterglow Band / [Peak] (nm)	Excitation Band / peak (nm)	Afterglow Duration	Reference
$Y_3Sc_2Ga_3O_{12}$	Ce^{3+}	Cr^{3+}	[500] (Green)	[400] (UV-VIS)	[1.5 h] R	1,2
$La_3Ga_5GeO_{14}$	Cr^{3+}	-	[700-1300] (NIR)	[240-480] (UV)	[8 h] R	3,6
$Zn_3Ga_2Ge_2O_{10}$	Cr^{3+}	-	[650-1000] (NIR)	[300-600] (UV-VIS)	[360 h] R	7,8
$LiGa_5O_8$	Cr^{3+}	-	[600-850] (NIR)	[250-350] (UV)	[1000 h] R	9-11
$SrGa_2O_4$	Cr^{3+}	-	[850-950] (NIR)	[254] (UV)	[2 h] R	12
$MgGa_2O_4$	Cr^{3+}	-	[650-770] (NIR)	X-ray (HR)	[30 h] R	13
$Zn_3Ga_2SnO_8$	Cr^{3+}	-	[650-1000] (NIR)	[300-600] (UV-VIS)	[300 h] R	14
$ZnGa_2O_4$	Cr^{3+}	-	[600-800] (NIR)	[250-600] (UV-VIS)	[5 h] R	3, 15-20
$Ca_3Ga_2Ge_3O_{12}$	Cr^{3+}	Yb^{3+}, Tm^{3+}	[650-850] (NIR)	[250-400] (UV-VIS)	[2.0 h] R	21,22
$La_3GaGe_5O_{16}$	Cr^{3+}	-	[650–750] (NIR)	[310–570] (UV–VIS)	[0.5 h] R	23
$BaLu_2Al_2Ga_2SiO_{12}$	Cr^{3+}	Tb^{3+}	[700] (NIR)	[440-600] (VIS)	[24 h] R	24
$Gd_3Al_{5-x}Ga_xO_{12}$	Cr^{3+}	Eu^{3+}	[690–720] (NIR)	[250–620] (UV–VIS)	[1 h] R	25
$Ca_{14}Zn_6Ga_{10}O_{35}$	Cr^{3+}	-	[650–750] (NIR)	[250–540] (UV–VIS)	[3 h] R	26
β-Ga_2O_3	Cr^{3+}	-	[650–850] (NIR)	[280–360] (UV)	[4 h] R	27

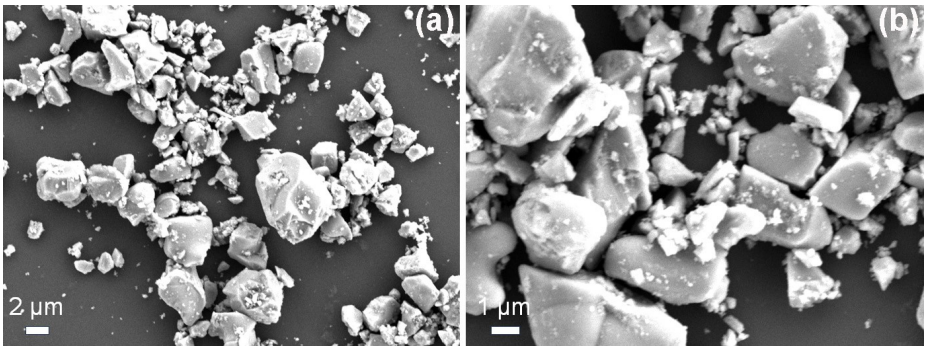

Fig. S1. SEM images of ZGO:0.5%Cr^{3+},0.5%Bi^{3+} phosphor.

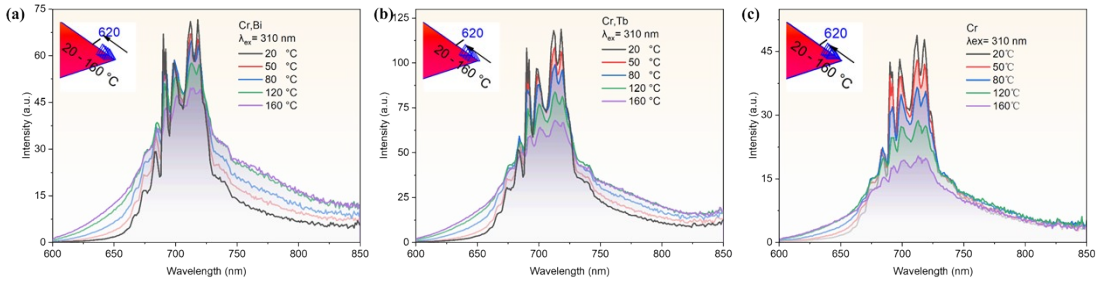

Fig. S2. Temperature-dependent PL properties and their CIE chromaticity coordinate of ZGO:0.5%Cr^{3+},0.5%M^{3+} (M = Bi, Tb) and ZGO:0.5%Cr^{3+} phosphors under 310 nm UV light excitation. (a) ZGO:0.5%Cr^{3+},0.5%Bi^{3+}, (b) ZGO:0.5%Cr^{3+},0.5%Tb^{3+}, (c) ZGO:0.5%Cr^{3+}. The CIE chromaticity coordinate insets of (a–c) indicate the evolution trend of emission color as a function of temperature.

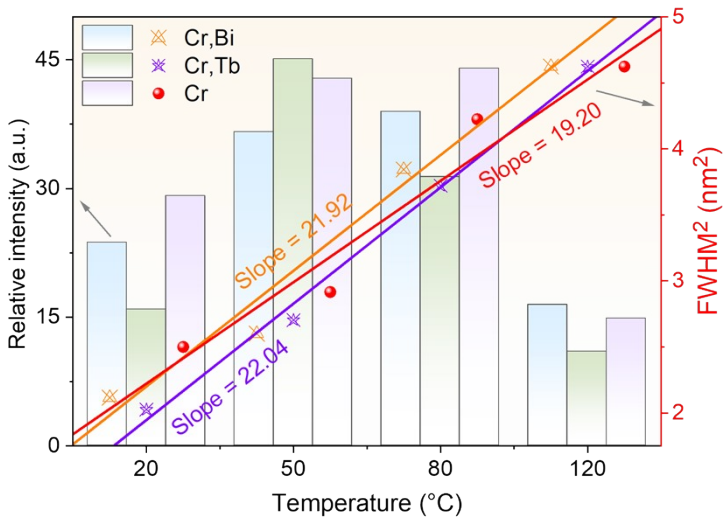

Fig. S3. The relative PersL intensity and $FWHM^2$ of the PersL peaks for ZGO:0.5%Cr^{3+},0.5%M^{3+} (M = Bi, Tb) and ZGO:0.5%Cr^{3+} phosphors as a function of temperature (the data are from Fig. 3c-e).

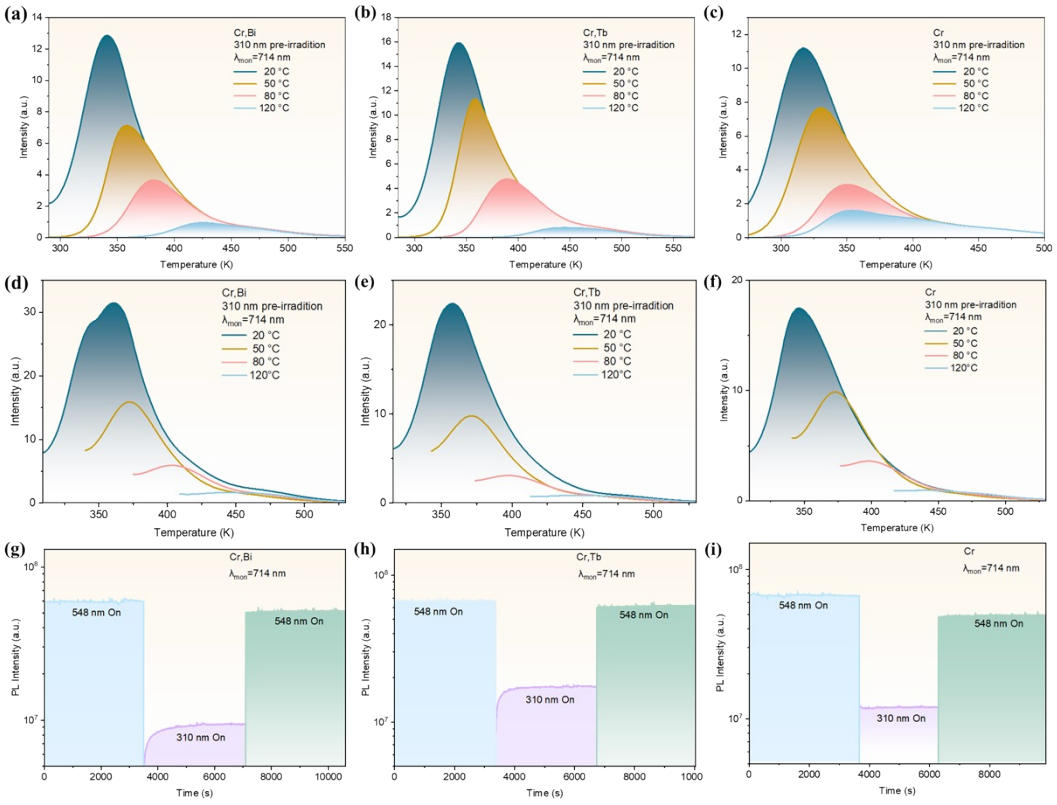

Fig. S4. Temperature-dependent TL curves and dynamic PL response of ZGO:0.5%Cr^{3+},0.5%M^{3+} (M = Bi, Tb) and ZGO:0.5%Cr^{3+} phosphors. (a-c) TL T_{STOP} curves measured by charging the sample at the heating temperature, turning off the light source, allowing the trap energy levels of the system to relax and recover to RT, and then starting the TL measurement (T_{STOP} at 20 °C, 50 °C, 80 °C, and 120 °C). (d-f) TL curves acquired by charging the sample at the heating temperature, then turning off the light source and initiating the test from the heating temperature (T_{Start} at 20 °C, 50 °C, 80 °C, and 120 °C). (g-i) Dynamic PL process under alternating irradiation of 310 nm and 548 nm light. Prior to TL measurements, the samples were charged with 310 nm UV light for 5 minutes. The monitoring wavelength was fixed at 714 nm for all measurements.

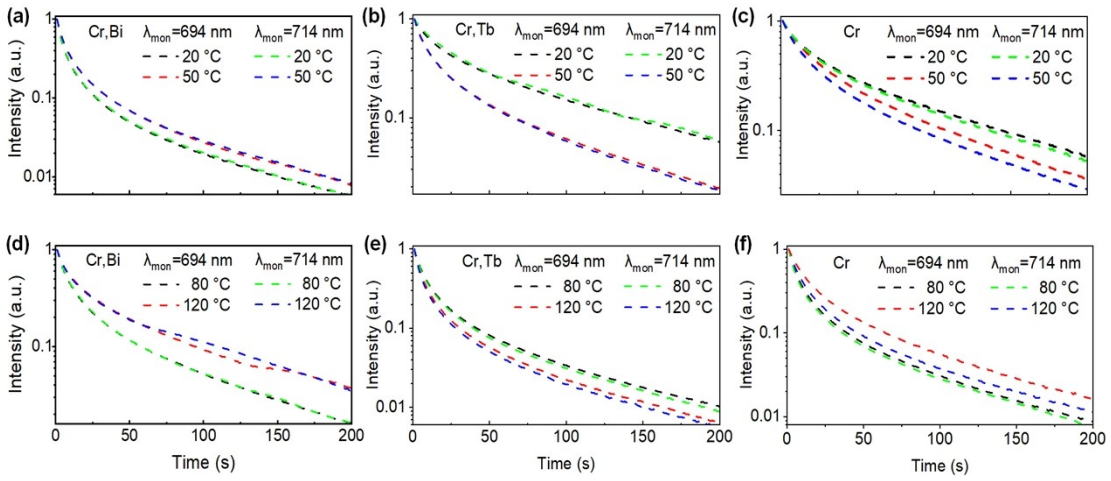

Fig. S5. Temperature-dependent PersL decay curves of ZGO:0.5% Cr^{3+}, 0.5% M^{3+} (M = Bi, Tb) and ZGO:0.5%Cr^{3+} phosphors. (a,d) ZGO: 0.5%Cr^{3+},0.5%Bi^{3+}. (b,e) ZGO: 0.5%Cr^{3+},0.5%Tb^{3+}. (c,f) ZGO: 0.5%Cr^{3+}. Prior to measuring the PersL decay curves, all phosphors were pre-irradiated with 310 nm UV light for 5 min.

Table S2. Temperature-dependent PersL lifetime of ZGO:0.5% Cr^{3+}, 0.5% M^{3+} (M = Bi, Tb) and ZGO:0.5%Cr^{3+} phosphors. (the data are from Figs. 3g-i).

Parameter / sample	Temperature (℃)	A_1 (*10^7)	A_2 (*10^7)	A_3 (*10^7)	τ_1 (s)	τ_2 (s)	τ_3 (s)
ZGO:Cr^{3+},Bi^{3+}	20	1.407	1.831	1.103	9.029	38.889	187.321
	50	5.502	4.844	1.635	5.133	24.169	127.373
	80	3.490	2.486	0.688	6.346	25.907	131.389
	120	1.694	1.343	0.326	4.349	18.565	101.160
ZGO:Cr^{3+},Tb^{3+}	20	1.362	1.637	0.918	8.340	36.254	178.509
	50	3.615	3.028	1.040	6.462	27.101	135.013
	80	4.406	2.729	0.703	3.963	17.030	98.643
	120	1.655	1.228	0.245	2.970	14.479	91.101
ZGO:Cr^{3+}	20	0.023	1.072	0.495	7.311	37.795	209.478
	50	0.023	7.245	0.210	34.157	35.160	563.029
	80	0.080	9.203	0.319	21.780	21.780	235.414
	120	1.682	0.753	0.239	18.278	18.290	108.400

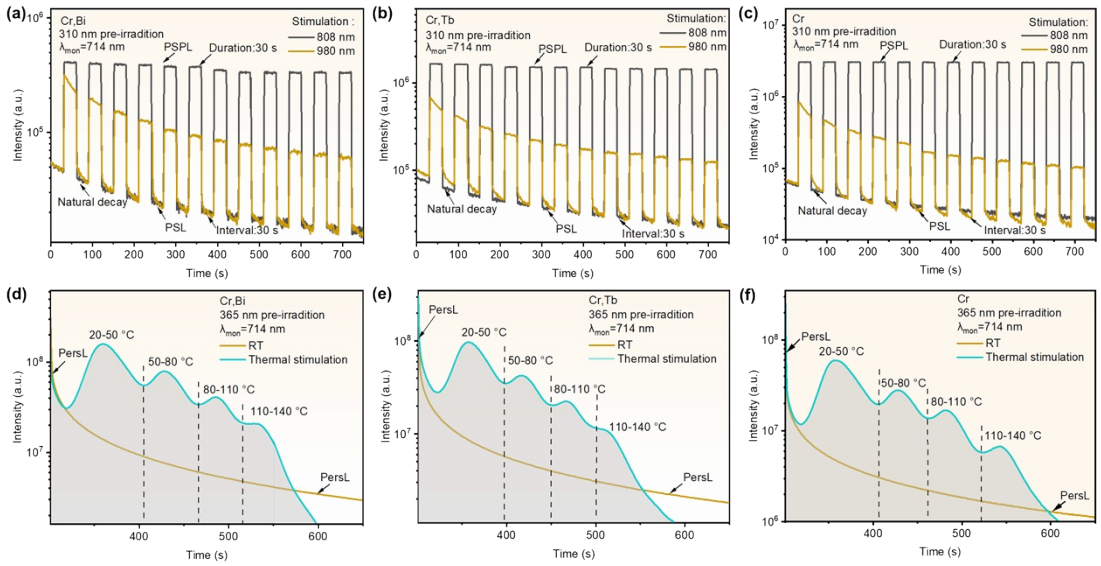

Fig. S6. PSL and TSL properties of ZGO:0.5%Cr^{3+},0.5%M^{3+} (M = Bi, Tb) and ZGO:0.5%Cr^{3+}. (a–c) PSL decay curves recorded under repeated infrared laser stimulation (808 and 980 nm, 0.25 W, 30 s on/off cycles) after pre-irradiation with 310 nm excitation. (d–f) TSL glow curves measured after 365 nm UV pre-irradiation for 5 min. Natural decay processes are also shown for comparison. The emission was monitored at 714 nm, and characteristic temperature regions of trap release are indicated.

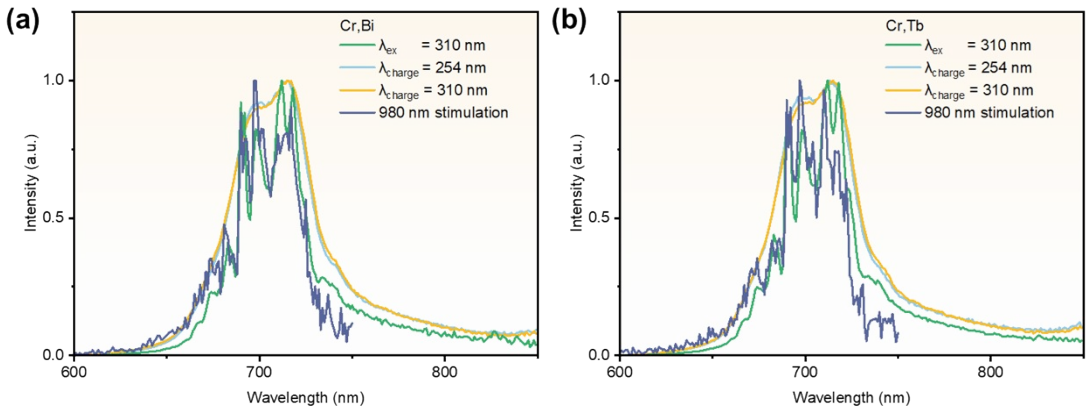

Fig. S7. PL and PersL spectra of ZGO:0.5%Cr^{3+},0.5%M^{3+} (M = Bi, Tb) under different excitation conditions. (a) ZGO:0.5%Cr^{3+},0.5%Bi^{3+}; (b) ZGO:0.5%Cr^{3+},0.5%Tb^{3+}. The spectra include PL measured under continuous 310 nm excitation and 980 nm infrared stimulation, and PersL recorded after charging with 254 nm or 310 nm UV irradiation. All characteristic emissions are assigned to Cr^{3+} centers.

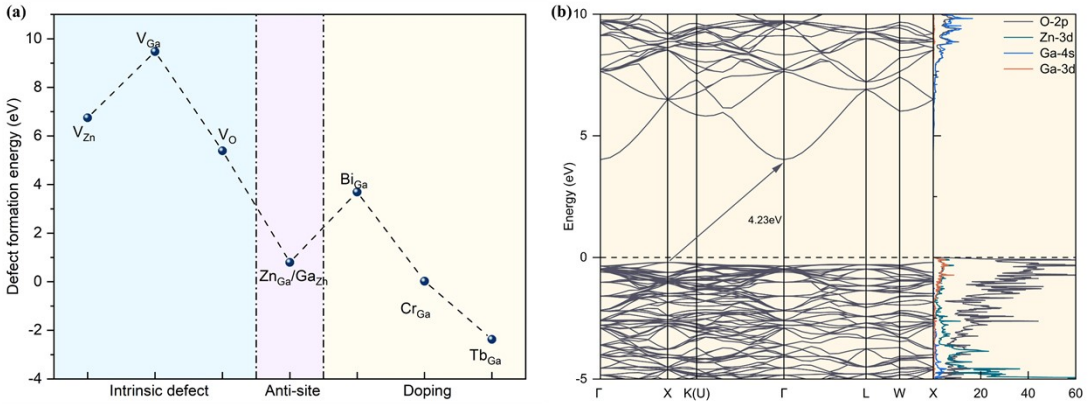

Fig. S8. Defect formation energies, band structures and PDOS of ZGO. (a) Relative formation energies of intrinsic defects (V_{Zn}, V_{Ga}, V_O), anti-site defects (Zn_{Ga}/Ga_{Zn}), and doping defects (i.e., Cr_{Ga}, Bi_{Ga}, Tb_{Ga}) calculated using the PBE functional. (b) Band structure and projected density of states (PDOS) of pristine ZGO.

The formation energies of all the possible doping defects were calculated using the following equation:[28]

$$E_{\text{form}} = E_{\text{doped}} - E_{\text{pure}} - \text{n}E_{\text{dopant}} + \text{m}E_{\text{atom}} \quad (1)$$

where E_{doped} and E_{pure} are the total energies of the doped and undoped samples, respectively. E_{dopant} and E_{atom} represent isolated atomic energies of the dopant atom and the atom replaced dopant; n and m stand for the number of the dopants (Bi/Tb/Cr) and the Ga atoms replaced by Bi/Tb/Cr, respectively.

Table S3. Total energies and relative substitution energies of pristine, intrinsic-defect, anti-site-defect, and doped ZGO conventional unit cell calculated using the PBE functional.

Material	Pristine	V_{Zn}	V_{Ga}	V_O	Zn_{Ga}/Ga_{Zn}	Cr_{Ga}	Bi_{Ga}	Tb_{Ga}
Total Energy (eV)	-317.81	-309.80	-305.42	-308.12	-317.01	-315.07	-321.40	-329.29
E_{form} (eV)		6.75	9.48	5.39	0.80	0.02	0.62	-3.69

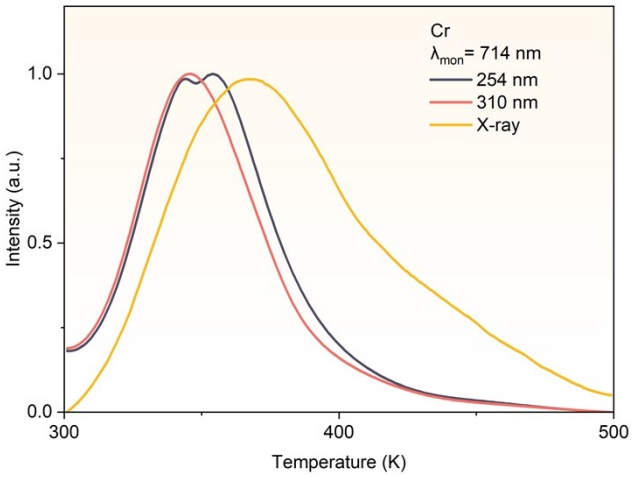

Fig. S9. Normalized TL curves of ZGO:0.5%Cr^{3+} charging at 254 nm, 310 nm UV light and X-rays. Note that TL curves acquired at 2 days after X-ray irradiation and the residual TL curves obtained after 30 s of charging.

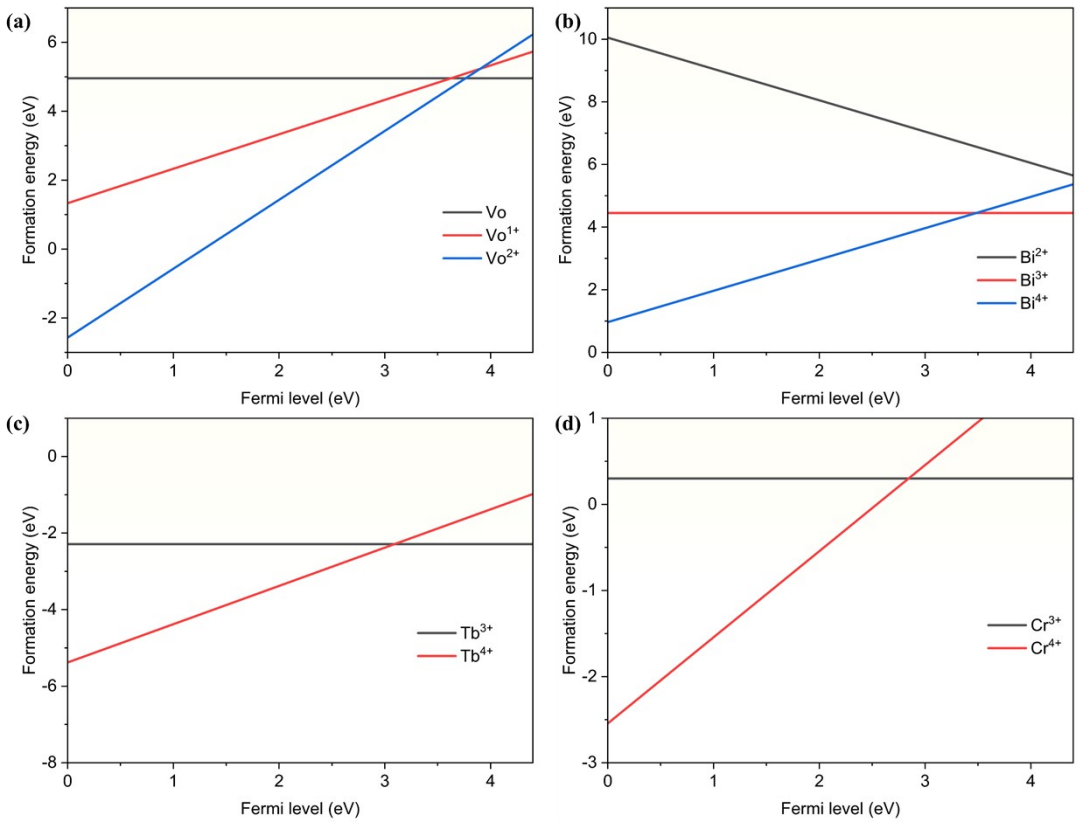

Fig. S10. Calculated formation energies of intrinsic oxygen vacancies and dopants in different valence states versus the Fermi level. The VBM is taken as the reference. (a) V_O in charge states 0, +1, and +2; (b) Bi_{Ga} in charge states +2, +3, and +4; (c) Tb_{Ga} in charge states +3 and +4; (d) Cr_{Ga} in charge states +3 and +4. Note that formation energies were calculated following the standard charged-defect formalism, with the chemical potentials of constituent elements. The Fermi level range is constrained by the band gap of ZGO.

The formation energies of defects are calculated by the following formula:

$$E_F(M^{q+x}) = E^q(M) - E(ZGO) - \mu_M + \mu_{Ga} + q\varepsilon f$$

where E (ZGO) and E^q(M) are the total energies of ZGO without and with defects, M (M = Cr, Bi or Tb), μ_M and μ_{Ga} are the chemical potentials of the bulk M and Ga, q is the net charge of the defective system, and q + x is the valence state of the M ion. In

the case of a neutral system, the M ion should be in the 3+ state since it replaces the Ga^{3+} ion in our structural model. When x electrons are added to the system, the net charge of the system (q) is −x, and the valence state of the M ion becomes 3 + x. εf is the chemical potential of an electron, which is equivalent to the Fermi level. The results presented in Fig. S10 illustrate the thermodynamic stability of different charge states under varying Fermi levels, thereby providing key insights into defect energetics and potential charge compensation mechanisms in doped ZGO systems.

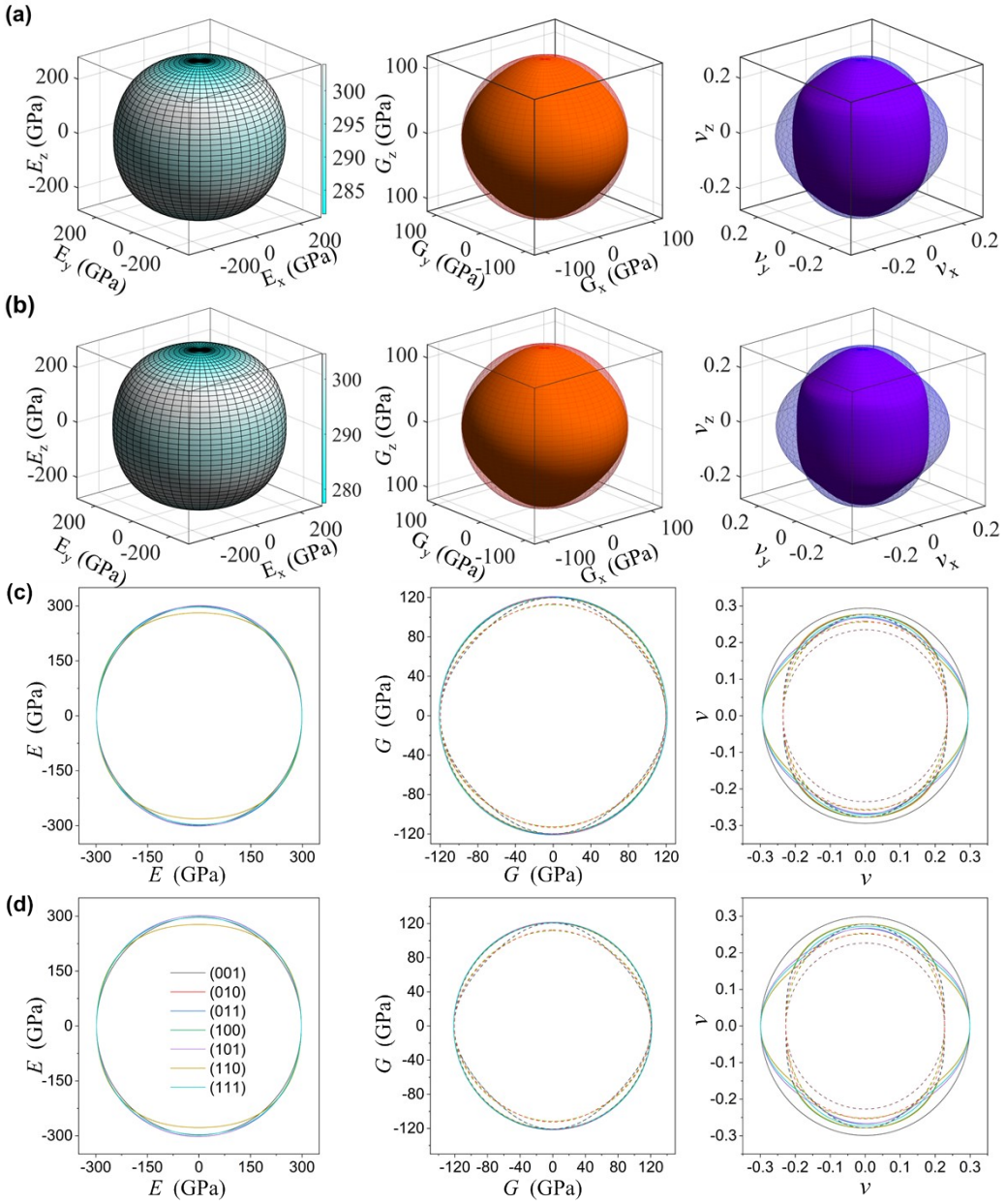

Fig. S11. Direction dependent 3D and 2D views of *E*, *G* and *v* for ZGO:Bi^{3+} and ZGO:Tb^{3+}. (a,c) 3D and 2D views in ZGO:Bi^{3+}. (b,d) 3D and 2D views in ZGO:Tb^{3+}.

Table S4. The Maximum and minimum elastic modulus and their ratio in different planes of pure ZGO (denoted as ZGO), ZGO:Bi^{3+} (denoted as Bi_{Ga}), ZGO:Cr^{3+} (denoted as Cr_{Ga}) and ZGO:Tb^{3+} (denoted as Tb_{Ga}).

		E_{max}	E_{min}	ratio	G_{max}	G_{min}	ratio	ν_{max}	ν_{min}	ratio
ZGO	(100)	290.83	252.93	1.15	122.65	97.90	1.25	0.34	0.19	1.79
	(010)	290.83	252.93	1.15	122.65	97.90	1.25	0.34	0.19	1.79
	(001)	290.83	252.93	1.15	122.65	97.90	1.25	0.34	0.19	1.79
	(011)	306.12	252.93	1.21	122.65	97.90	1.25	0.34	0.19	1.79
	(101)	306.12	252.93	1.21	122.65	97.90	1.25	0.34	0.19	1.79
	(110)	306.12	252.93	1.21	122.65	97.90	1.25	0.34	0.19	1.79
	(111)	290.83	290.83	1.00	122.65	97.90	1.25	0.34	0.19	1.79
	whole	306.10	252.93	1.21	122.65	97.91	1.25	0.34	0.19	1.79
Bi_{Ga}	(100)	304.01	281.40	1.08	121.03	112.66	1.07	0.29	0.23	1.26
	(010)	303.01	281.40	1.08	121.03	112.67	1.07	0.29	0.23	1.26
	(001)	298.42	298.42	1.00	121.03	119.64	1.01	0.29	0.23	1.26
	(011)	303.88	298.42	1.02	121.03	112.67	1.07	0.29	0.23	1.26
	(101)	303.69	298.34	1.02	120.98	112.67	1.07	0.29	0.23	1.26
	(110)	303.72	298.40	1.08	120.97	112.67	1.07	0.29	0.23	1.26
	(111)	302.41	297.20	1.02	121.03	112.66	1.07	0.29	0.23	1.26
	whole	304.00	281.40	1.08	121.03	112.66	1.07	0.29	0.23	1.26
Cr_{Ga}	(100)	428.09	302.76	1.41	209.61	128.58	1.63	0.63	-0.06	-10.5
	(010)	428.02	304.20	1.41	209.60	128.58	1.63	0.63	-0.06	-10.5
	(001)	428.02	428.02	1.00	132.02	128.58	1.03	0.63	-0.06	-10.5
	(011)	428.02	303.71	1.41	209.61	128.58	1.63	0.63	-0.06	-10.5
	(101)	428.09	304.80	1.40	209.61	129.07	1.62	0.63	-0.06	-10.5
	(110)	428.06	303.18	1.41	209.61	128.79	1.63	0.63	-0.06	-10.5
	(111)	428.06	302.86	1.41	209.61	128.76	1.63	0.63	-0.06	-10.5
	whole	428.02	302.96	1.41	209.56	128.58	1.63	0.63	-0.05	-10.5
Tb_{Ga}	(100)	304.66	277.51	1.10	121.50	111.51	1.09	0.30	0.23	1.30
	(010)	304.08	277.51	1.10	121.50	111.51	1.09	0.30	0.23	1.30
	(001)	297.89	297.89	1.00	121.50	120.52	1.01	0.30	0.23	1.30
	(011)	304.55	297.89	1.02	121.50	111.51	1.09	0.30	0.23	1.30
	(101)	304.47	297.87	1.02	121.48	111.51	1.09	0.30	0.23	1.30
	(110)	304.49	277.51	1.10	121.47	111.51	1.09	0.30	0.23	1.30
	(111)	303.70	296.83	1.02	121.50	111.51	1.09	0.30	0.23	1.30
	whole	304.60	277.51	1.10	121.50	111.51	1.09	0.30	0.23	1.30

Table S5. The elastic constants C_{ij} (GPa) and *B*, *G*, *E*, and *v* (GPa), *H*, Zener ratio (A) and A^U for four models including pure ZGO (denoted as ZGO), ZGO:Bi^{3+}(denoted as Bi_{Ga}), ZGO:Cr^{3+} (denoted as Cr_{Ga}) and ZGO:Tb^{3+} (denoted as Tb_{Ga}).

Name	C_{11}	C_{12}	C_{13}	C_{14}	C_{33}	C_{44}	C_{66}	*B*	*G*	*E*	*B/G*	*v*	*H*	A	A^U
ZGO	333	137				123		202	112	284	1.81	0.27	12.72	1.25	0.06
Bi_{Ga}	369	127	137	-0.49	358	120	121	211	118	299	1.78	0.26	13.45	0.99	0.01
Cr_{Ga}	716	453	-62	-1.23	374	129	132	236	161	393	1.47	0.22	21.67	0.98	1.47
Tb_{Ga}	367	124	137	-0.29	354	121	121	209	118	299	1.77	0.26	13.66	1.00	0.01

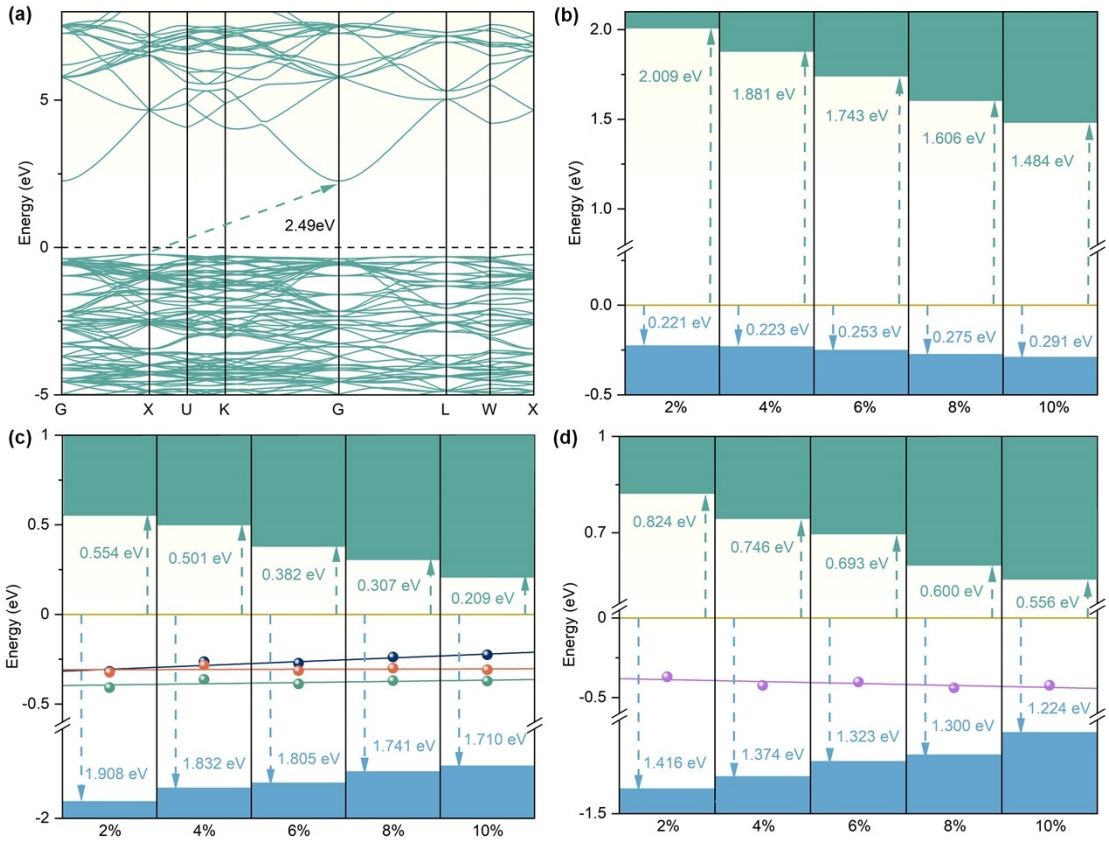

Fig. S12. The electron bandgap structures of pure ZGO and doped ZGO after applying uniaxial strain along the c direction. (a) Electron bandgap structure of pure ZGO; (b) Electron bandgap structure of pure ZGO under uniaxial strain along the c direction; (c) Electron bandgap structure of ZGO:Cr^{3+} under uniaxial strain along the c direction; (d) Electron bandgap structure of ZGO:Bi^{3+} under uniaxial strain along the c direction. The orange line in (b–d) represents the Fermi level, the spheres in (c) and (d) indicate the impurity bands, and the curves are the fitted curves of the impurity bands, green and blue squares represent the CB and VB, respectively.

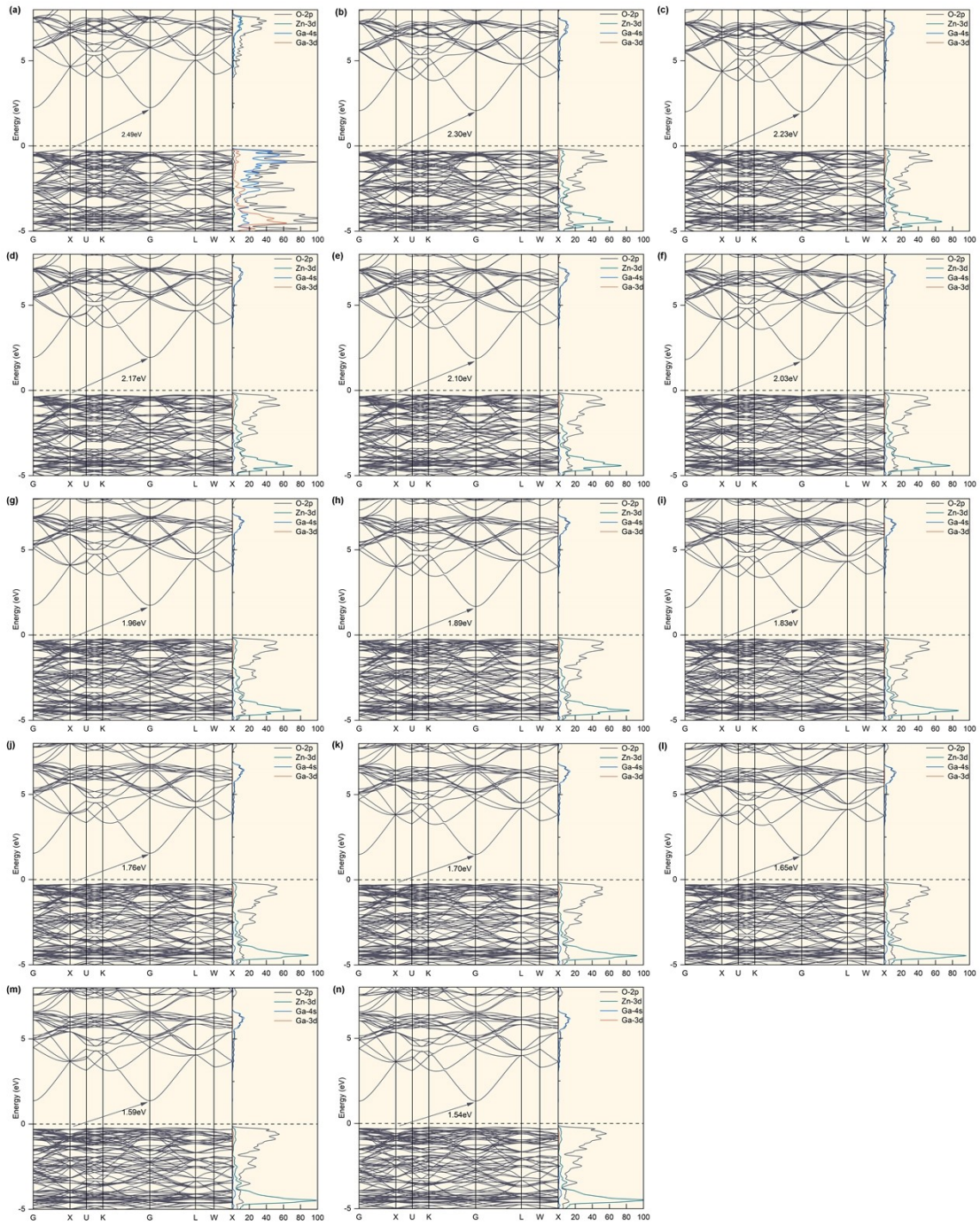

Fig. S13. The band structures and PDOS of pure ZGO under uniaxial strain along the c-axis. (a–n) correspond to strain levels from 0% to 13% with an interval of 1%.

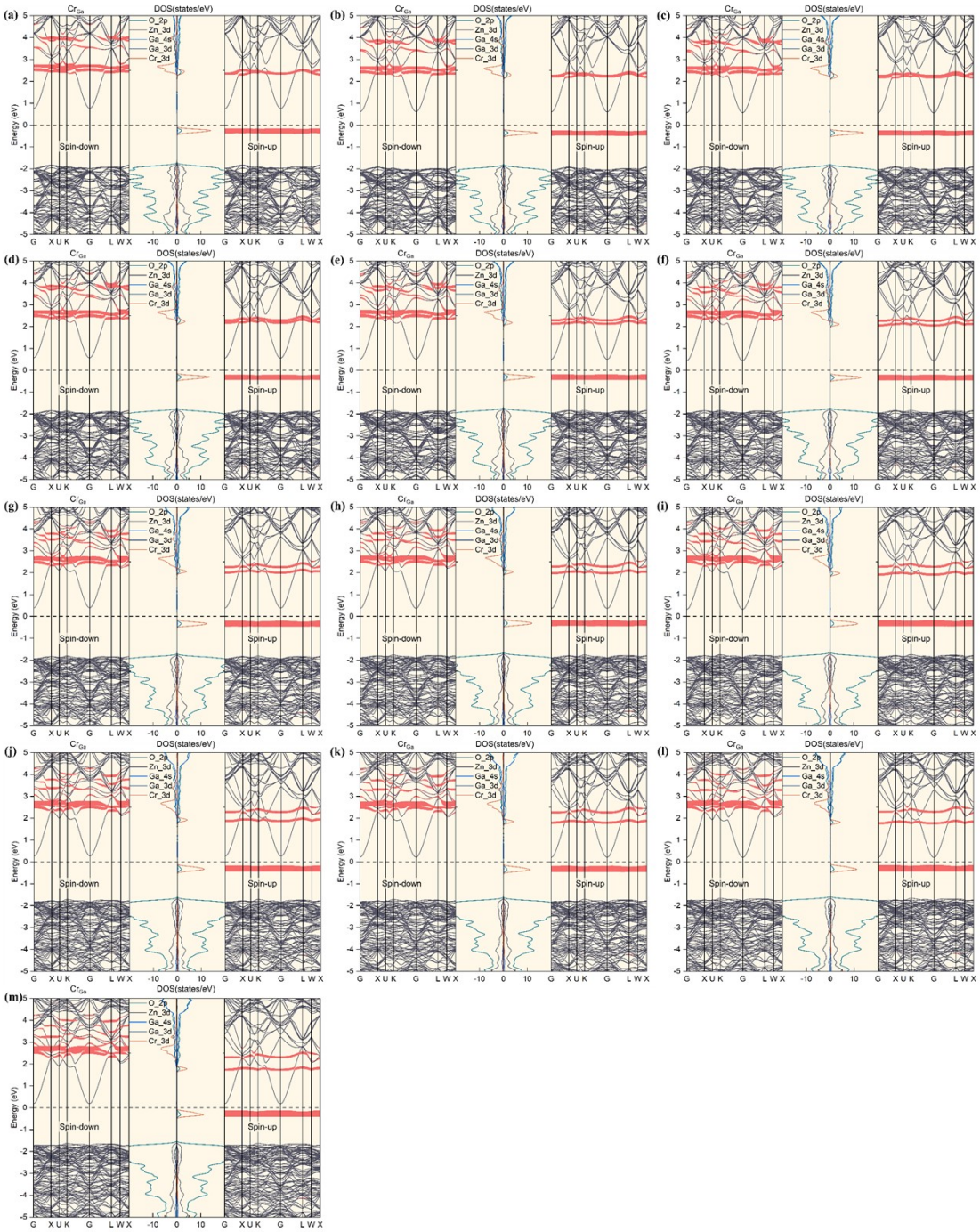

Fig. S14. The band structures and PDOS of ZGO:Cr^{3+} under uniaxial strain along the c-axis. (a–m) correspond to strain levels from 0% to 12% with an interval of 1%.

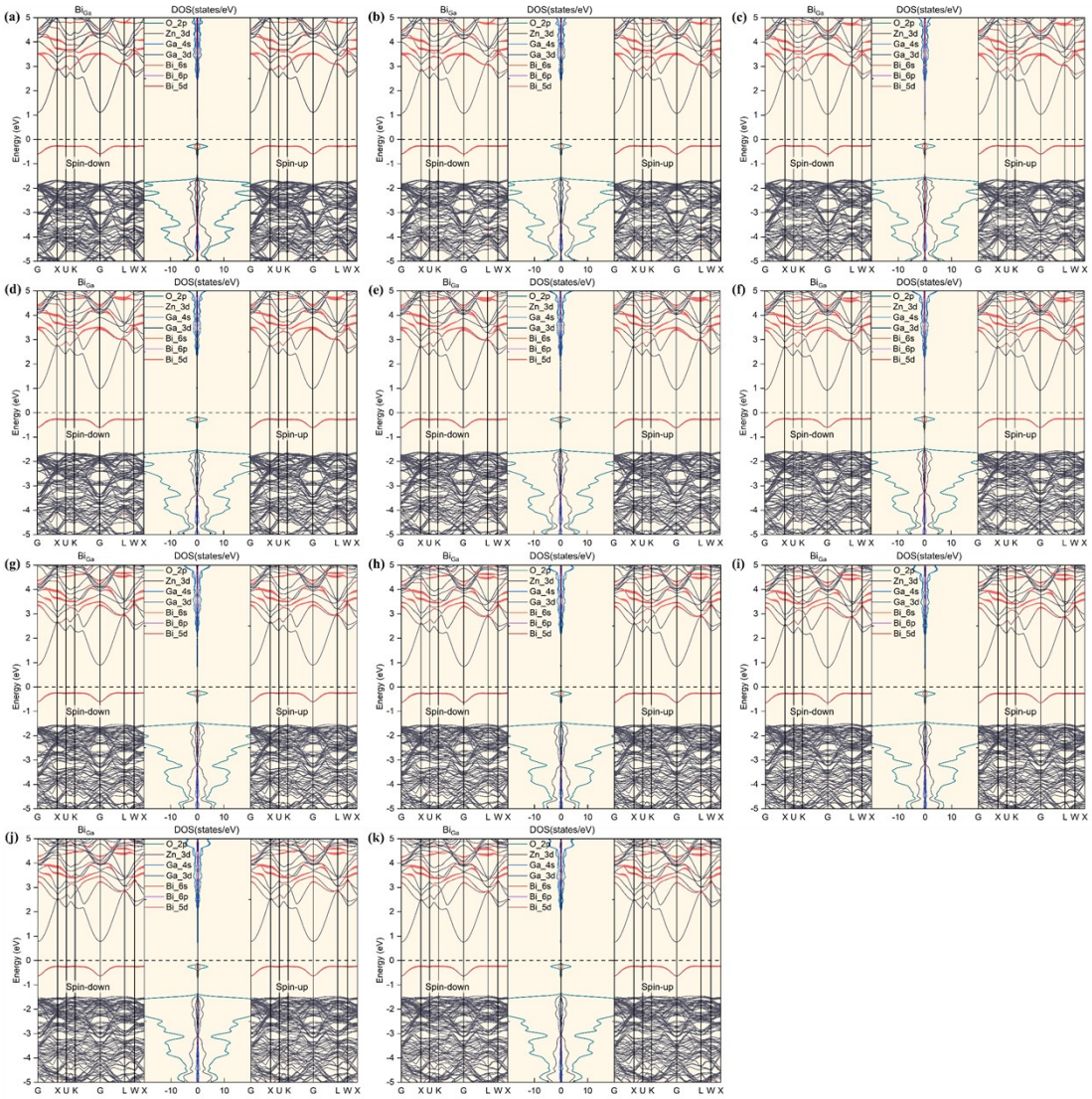

Fig. S15. The band structures and PDOS of ZGO:Bi^{3+} under uniaxial strain along the c-axis. (a–k) correspond to strain levels from 0% to 10% with an interval of 1%.

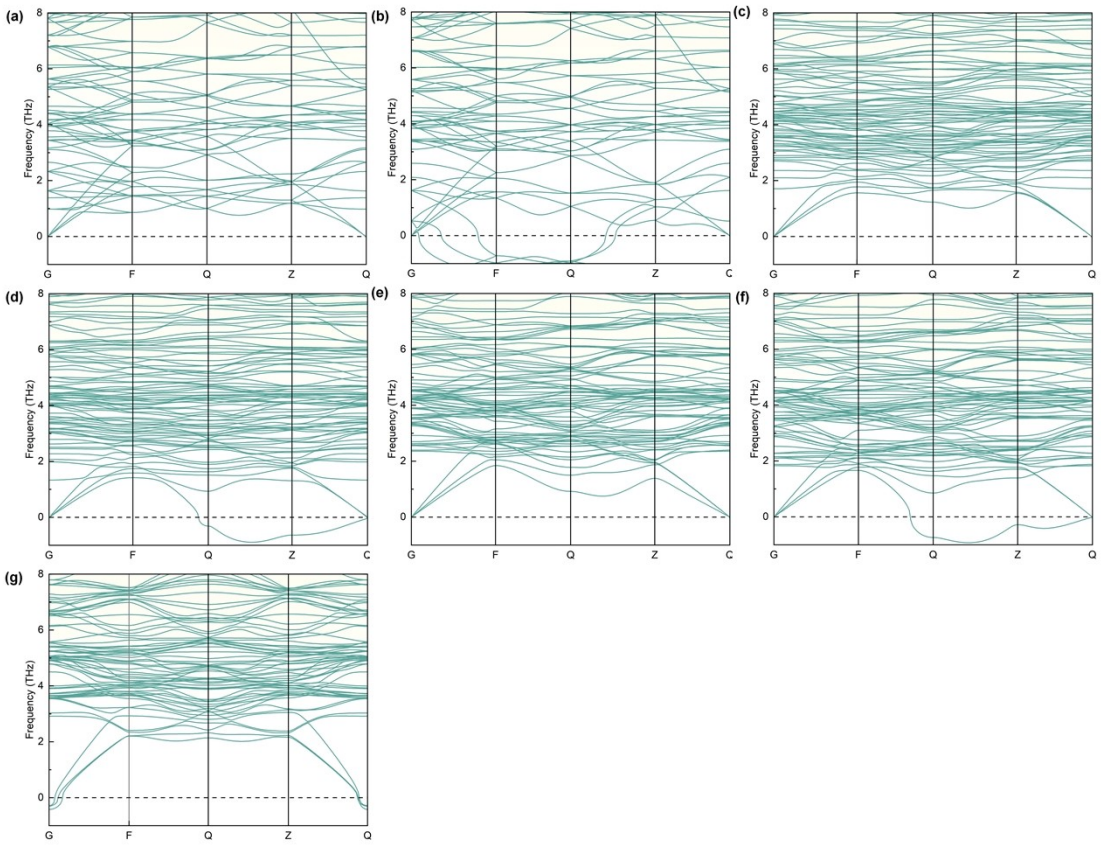

Fig. S16. Phonon spectra characterizing the stability of pure ZGO and doped ZGO under uniaxial strain along the c-axis. (a, b) Phonon spectra of pure ZGO under 13% and 14% uniaxial strains along the c-axis, respectively; (c, d) phonon spectra of ZGO:Bi^{3+} under 10% and 11% uniaxial strains along the c-axis, respectively; (e, f) phonon spectra of ZGO:Cr^{3+} under 13% and 14% uniaxial strains along the c-axis, respectively; (g) phonon spectra of ZGO:Tb^{3+} under 1% uniaxial strain along the c-axis.

References

1. Y. Luo, Z. Xia, *J. Phys. Chem. C* 2014, **118**, 23297
2. J. Ueda, K. Aishima, S. Nishiura, S. Tanabe, *Appl. Phys. Express* 2011, **4**, 042602.
3. Y. Zhuang, J. Ueda, S. Tanabe, P. Dorenbos, *J. Mater. Chem. C* 2014, **2**, 5502.
4. X. Yi, Z. Chen, S. Ye, Y. Li, E. Song, Q. Zhang, *RSC Adv*. 2015, **5**, 49680.
5. W. Yan, F. Liu, Y. Lu, X. Wang, M. Yin, Z. Pan, *Opt. Express* 2010, **18**, 20215.
6. D. Jia, L. Lewis, X. Wang, *Electrochem. Solid St*. 2010, **13**, J32.
7. Z. Pan, Y. Lu, F. Liu, *Nat. Mater*. 2011, **11**, 58.
8. Y. Wu, Y. Li, X. Qin, R. Chen, D. Wu, S. Liu, J. Qiu, *Spectrochim. Acta A* 2015, **151**, 385.
9. F. Liu, W. Yan, Y. Chuang, Z. Zhen, J. Xie, Z. Pan, *Sci. Rep.* 2013, **3**, 1554.
10. Y. Chuang, Z. Zhen, F. Zhang, F. Liu, J. Mishra, W. Tang, H. Chen, X. Huang, L. Wang, X. Chen, J. Xie, Z. Pan, *Theranostics* 2014, **4**, 1112.
11. D. Chen, J. Eur. Ceram. Soc. 2014, **34**, 4069.
12. N. Basavaraju, K. Priolkar, D. Gourier, S. Sharma, A. Bessiere, B. Viana, *Phys. Chem. Chem. Phys*. 2015, **17**, 1790.
13. N. Basavaraju, K. Priolkar, D. Gourier, A. Bessiere, B. Viana, Phys. *Chem. Chem. Phys*. 2015, **17**, 10993.
14. Z. Zou, J. Wu, H. Xu, J. Zhang, Z. Ci, Y. Wang, *J. Mater. Chem. C* 2015, **3**, 8030.
15. M. Allix, S. Chenu, E. Véron, T. Poumeyrol, E. Kouadri-Boudjelthia, S. Alahraché, F. Porcher, D. Massiot, F. Fayon, *Chem. Mater*. 2013, **25**, 1600.
16. A. Bessière, S. Sharma, N. Basavaraju, K. Priolkar, L. Binet, B. Viana, A. Bos, T. Maldiney, C. Richard, D. Scherman, D. Gourier, *Chem. Mater*. 2014, **26**, 1365.
17. D. Gourier, A. Bessière, S. Sharma, L. Binet, B. Viana, N. Basavaraju, K. Priolkar, *J. Phys. Chem. Solids* 2014, **75**, 826.
18. D. Li, Y. Wang, K. Xu, H. Zhao, Z. Hu, *RSC Adv*. 2015, **5**, 20972.
19. Y. Zhuang, J. Ueda, S. Tanabe, *J. Mater. Chem. C* 2013, **1**, 7849.
20. A. Bessiere, S. Jacquart, K. Priolkar, A. Lecointre, B. Viana, D. Gourier, *Opt. Express* 2011, **19**, 10131.
21. D. Chen, Y. Chen, H. Lu, Z. Ji, *Inorg. Chem*. 2014, **53**, 8638.
22. C. Liu, Z. Xia, M. Molokeev, Q. Liu, H. Guo, *J. Am. Ceram. Soc*. 2015, **98**, 1870.
23. S. Zhang, Y. Hu, L. Chen, Y. Fu, G. Ju, *Opt. Mater. Express* 2016, **6**, 1247.
24. W. Yuan, R. Pang, S. Wang, T. Tan, J. Su, X. Chen, S. Zhang, H. Zhang, *Chem. Eng. J*. 2024, **481**, 148071.
25. J. Xu, J. Ueda, S. Tanabe, *Opt. Mater. Express* 2015, **5**, 963.
26. F. Sun, R. Xie, L. Guan, C. Zhang, *J. Lumin*. 2016, **180**, 251.
27. Y. Lu, F. Liu, Z. Gu, Z. Pan, *J. Lumin*. 2011, **131**, 2784.
28. J. Kim, H. Kang, W. Kim, J. Kim, J. Choi, H. Park, G. Kim, T. Kim, Y. Hwang, S. Mho, M. Jung, M. Han, *Appl. Phys. Lett*. 2003, **82**, 2029.